



OPEN Unique roll clouds along the flow path of the Indian summer monsoon low-level jet over the Arabian sea

B. Swathi^{1,2} & V. Sathiyamoorthy¹✉

Unique boundary layer roll clouds in the form of parallel straight lines are formed along the flow path of the Arabian Sea branch (ASB) of the Indian summer monsoon low-level jet. An attempt has been made in this study to understand the mechanism behind their formation using high-resolution NOAA-20 satellite imageries and ECMWF reanalysis data. Thermal and dynamical instabilities generated by the ASB of the low-level jet in the atmospheric boundary layer produce eddies in the primary flow of the ASB which organize themselves as counter rotating roll vortices. Roll clouds form over ascending regions of these vortices and clear-sky condition prevails over descending regions. Bulk Richardson number computed between 1000 hPa and 975 hPa levels highlight the instability regimes that support the formation of roll clouds. They are formed far away from the Western Ghats mountain without the orographic lifting of monsoon winds. These small-scale clouds are advected by the ASB, evolve into broken line clouds and further grow into closed convective cloud cells. Contribution of these roll clouds to the Indian summer monsoon activity is also discussed.

Keywords Roll clouds, Roll vortices, Indian summer monsoon, Low-level jet, Bulk Richardson number

An important component of the Indian summer monsoon circulation is the lower tropospheric southwesterly jet stream. It originates from southern hemispheric trade winds, crosses the equator along the east African coast, subsequently flows over the Arabian Sea, Indian Peninsula, Bay of Bengal and beyond^{1–4}. It is present during the Indian summer monsoon season of June to September (JJAS). Core of this low-level jet stream is found at 1.5 km above the surface over the Indian Peninsula². Seasonal mean peak strength of this jet at 850 hPa is about 18 ms^{-1} in the core region⁵. This jet is referred by different names in literature viz., Findlater jet, Somali jet, or Low-Level Jet (LLJ). Two important mechanisms were suggested regarding the formation of the LLJ during JJAS. They are (i) meridional pressure gradient arising due to land-sea thermal contrast prevailing between the heated Asian landmass and relatively cooler ocean south of it¹ (thermally driven) and (ii) northward migration of the Inter Tropical Convergence Zone (ITCZ) over the Indian monsoon region and associated latent heat release³ (convectively driven).

During its journey, LLJ carries moisture from the Indian Ocean and the Arabian Sea to Indian monsoon region. Strength of the LLJ and the moisture carried by it are closely linked to the monsoon activity^{6–8}. LLJ encounters north-south oriented Western Ghats mountain chain of peninsular India during its journey towards India. Orographic lifting of moist air carried by the LLJ causes cooling and saturation leading to widespread rainfall on the windward side of the Western Ghats^{9–13}. Recent studies pointed out that the core height of the LLJ is not confined to 850 hPa but found to vary from 950 hPa to 800 hPa over different parts of the Indian monsoon region¹⁴. Core height is at a relatively lower elevation of 950 hPa off Somalia and Saudi Arabian coasts, at 850 hPa over the Indian Peninsula and at 800 hPa over the Western Ghats mountain. Studies suggest that low level summer monsoon circulation (i.e., LLJ) is broadly organized into Arabian Sea, Bay of Bengal and south China Sea branches and these branches has its own characteristics¹⁵. Several studies have investigated the Bay of Bengal branch (B3) and its role in rainfall over India^{16–18}. But Arabian Sea branch (ASB) of the LLJ is less explored.

Various types of low-, mid- and high-level clouds are present over the Indian summer monsoon region during JJAS¹⁹. An interesting type of low-level boundary layer clouds known as roll clouds form over the Arabian Sea during this season. They appear as lines of cumulus/stratocumulus clouds. They are seen as parallel straight-line

¹Space Physics Laboratory, Vikram Sarabhai Space Centre (ISRO), Thiruvananthapuram, India. ²Department of Physics, University of Kerala, Thiruvananthapuram, India. ✉email: v.sathiyamoorthy@gmail.com; sathiyamoorthy@vssc.gov.in

clouds or string of pearls (composed of discrete cloud elements) in satellite imageries. Most of the roll cloud occurrences are reported over mid- and high-latitude oceans during cold-air outbreak events^{20,21}. The presence of roll clouds in the atmospheric boundary layer is attributed to the presence of roll vortices. Winds in the atmospheric boundary layer can be decomposed into two components; mean flow (primary flow) and secondary flow. Roll vortices are secondary flows embedded within the mean flow and have the magnitude of around 7–10% of the mean flow²². The vertical wind shear in the boundary layer tries to rotate the air parcel about the mean wind direction and the mean wind pushes the air parcel along the direction of its motion^{23–26}. The combination of vertical wind shear and the translational motion of the mean wind generates helical roll motion, resulting in counter-rotating roll vortices. These vortices have their axis parallel to the mean wind direction and consist of regions of alternating ascending and descending motions^{22,27,28}. A schematic of roll vortices in the atmospheric boundary layer is shown in Fig. 1.

The presence of roll vortices can be identified if there is some passive element serving as a visible marker. In the case of boundary layer roll vortices, water vapour condenses to form clouds over updraft regions and serves as a visible marker²². For the clouds to form and sustain over the updraft regions of the roll vortices, it is essential that the air is sufficiently moist and characterized by strong vertical ascent. Thermal instability strengthens the updraft regions. Thermal instability occurs when an atmospheric layer is heated from below or cooled from above. In case of cold-air outbreak over mid- and high-latitude regions, cold continental air flowing over relatively warmer water bodies creates thermally unstable conditions and leads to roll cloud formation. Therefore, both dynamic and thermal instabilities are required for the formation of boundary layer roll clouds, typically when the atmosphere is near-neutral to slightly unstable^{29–32}.

Over the Arabian Sea (located within the tropical belt), roll clouds are observed along the flow path of the ASB of the LLJ in satellite visible channel imageries during JJAS³³. These clouds (adjacent bands separated by a distance of about 10 km and stretching for about a few hundred km) cover a wide area of the Arabian Sea and adjoining India but failed to garner the attention of the meteorological community. Main reason for this is that these are low-level clouds, confined to the boundary layer and can't be distinguished from surface by infrared satellite imageries. One has to look for visible satellite imageries during day-time to observe these low-level clouds. Presence of mid- and high-level clouds obstructs the satellites from viewing these boundary layer roll clouds^{19,34}. One of the widely used methods for identifying roll clouds is visual inspection of visible channel satellite imageries. Although this approach is time-consuming, subjective and susceptible to human error, still it remains a widely used method for identifying roll clouds due to their unambiguous appearance in satellite visible channel imageries^{30,35,36}. For example, twenty-one roll cloud cases over the British Isles during March and April months of 1977 were studied using visible channel imageries from NOAA-5 satellite³⁷. Roll clouds over the Bering Sea during February to March 1975 were studied using NOAA-4 satellite photographs³⁸. In another study, 1446 roll cloud days over Greenland Sea and Barents Sea were studied using visual inspection of daily NOAA visible channel satellite imageries spanning 10 winters during 1985 to 1995 to generate the climatology of the clouds³⁵. Authors of this study stated that it is the most efficient and reliable method for detecting organized cloud structures in satellite images even though this method is time consuming. Himawari-8 satellite visible imageries were used to visually identify roll clouds over the Yellow Sea during cold air outbreaks in November 2015³⁹. Authors of this study pointed out that a direct method to objectively classify roll and non-roll cloud cases is unavailable and emphasized the need for further research in objective identification techniques and statistical analysis of roll cloud properties from satellite imageries.

One of the most consistent and visually recognizable features of roll clouds is their alignment along the mean wind direction in the atmospheric boundary layer^{20,21,29,30}. During the Indian summer monsoon season,

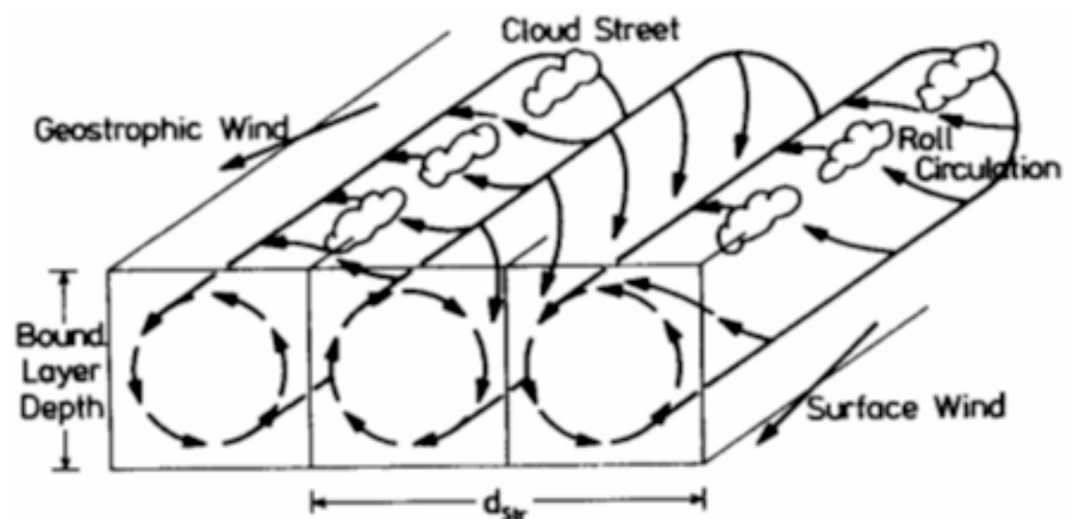


Fig. 1. Schematic diagram representing different processes involved in roll cloud formation in the boundary layer³⁵. d_{sr} is the wavelength of roll clouds.

the mean wind direction in the boundary layer over the Arabian Sea is southwesterlies, causing the roll clouds to align along southwest to northeast direction on the exit region of the ASB of the monsoon low level jet. This feature makes them identifiable in satellite imageries. Only a few observational studies of Arabian Sea roll clouds are available in the literature^{33,40}. Given the scope and constraints, roll clouds are visually identified from satellite visible channel imageries for the present study which align with the earlier studies. However, this subjective identification of roll clouds is bound to have human error. In the present study an effort is made to understand the formation mechanism of roll clouds over the Arabian Sea and their role in Indian summer monsoon activity.

Results

Characteristics of the monsoon low-level jet

Orographic set-up of the Indian summer monsoon region and its surrounding along with orographic elevation are presented in Fig. 2. Important mountains that interact with the low-level monsoon circulation over the east Africa, Saudi Arabian Peninsula and south Asia can be seen from this figure. It is reported that the LLJ is seen between the surface and ~ 700 hPa during the JJAS season³. Most studies consider 850 hPa as the representative lower tropospheric level to study the LLJ and hence characteristics of the LLJ at other levels are relatively less explored. As the literature¹⁴ suggest that the core height of the LLJ is found at 950 hPa over the west Arabian Sea, characteristics of the LLJ at both 950 hPa and 850 hPa levels are examined. In Fig. 3, ten-year (2005–2014) average horizontal winds at 950 hPa, 850 hPa and their difference during the JJAS season are shown. As pointed out by the earlier studies¹⁴, strongest winds of the LLJ are found at 950 hPa over the west Arabian Sea. Ten-year average seasonal mean peak wind speed at 950 hPa is 22 ms^{-1} and it is found close to the Horn of Africa. Wind speed contours of 950 hPa core over the west Arabian Sea are aligned in southwest to northeast direction.

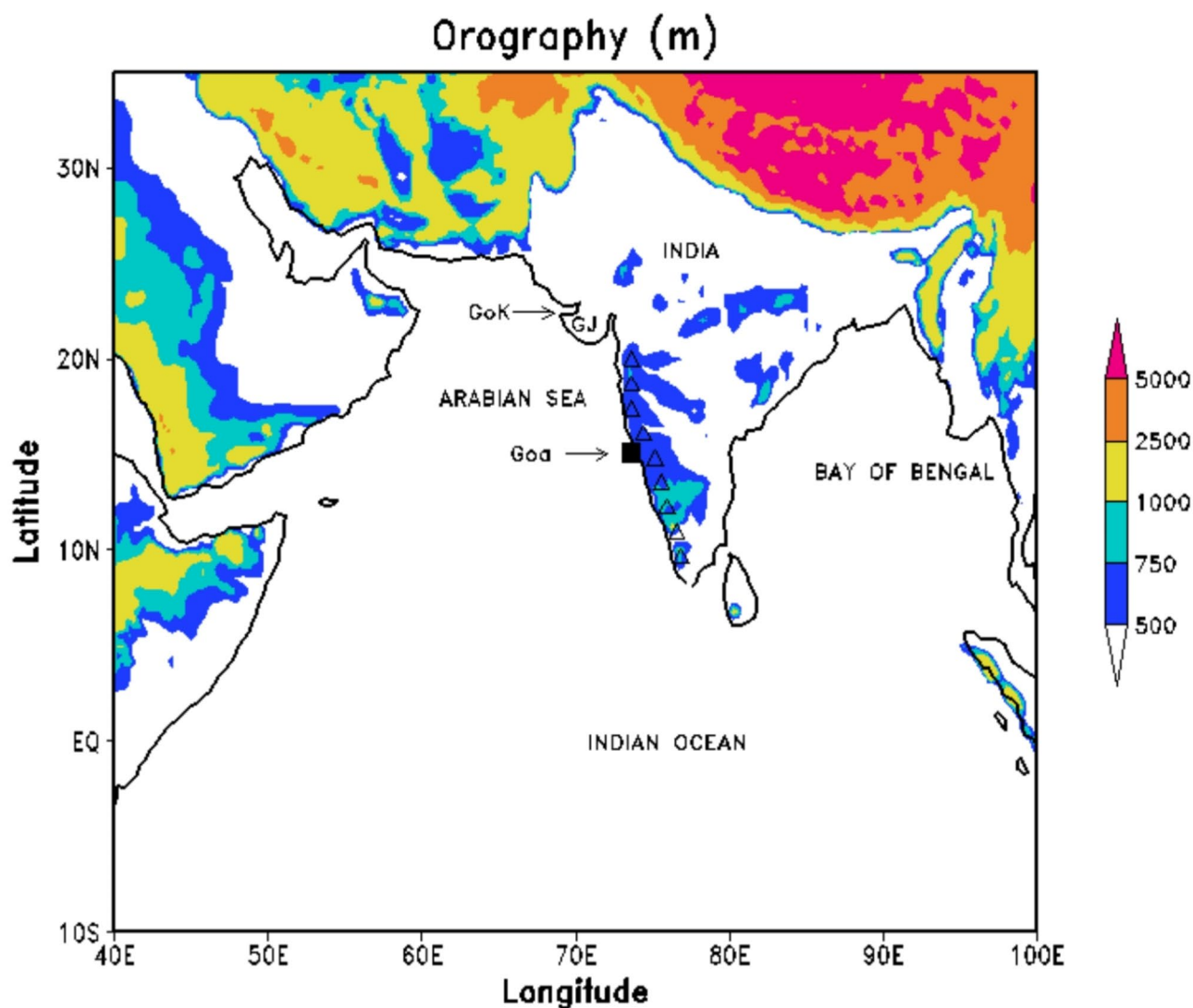


Fig. 2. Orographic set-up of the study region. Shades indicate orographic height in meters (uneven interval). Western Ghats mountain chain of west Peninsular India is highlighted with triangles. Letters 'GJ' show the Gujarat state of India. GoK is Gulf of Kutch. Location of Goa in the west coast of India is also shown.

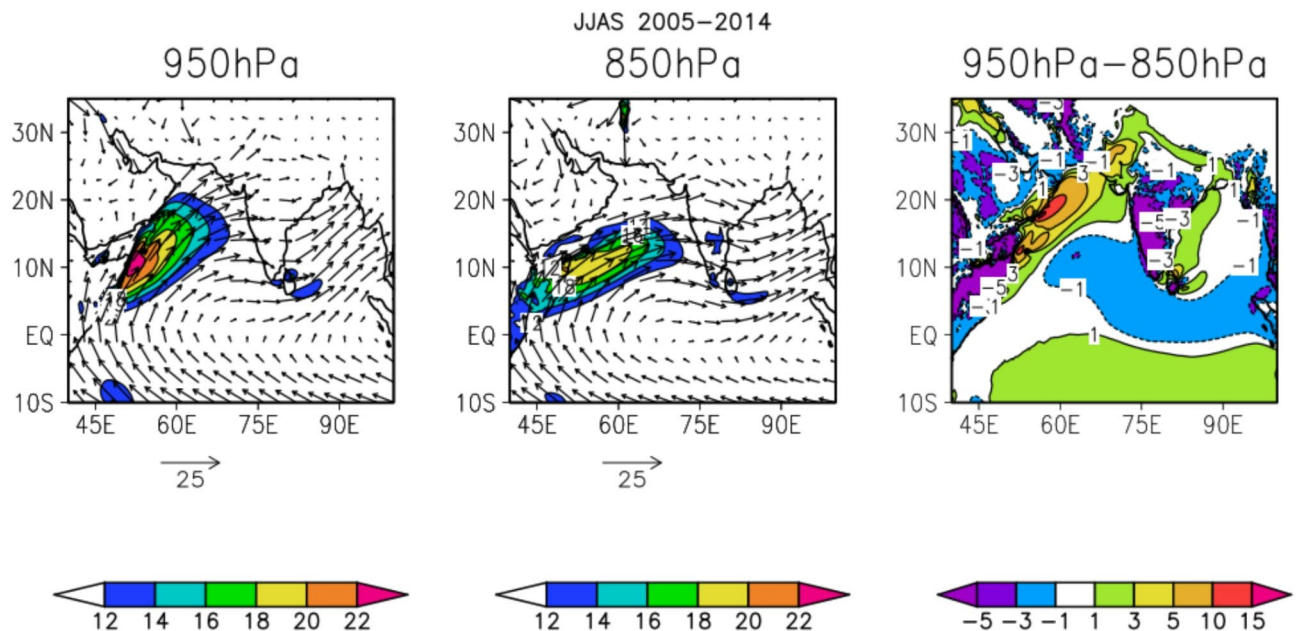


Fig. 3. Ten-year (2005–2014) average horizontal winds (ms^{-1}) during JJAS [speed as shades and contours overlaid with wind vectors] at 950 hPa, 850 hPa and wind speed difference between these two levels. Wind speeds above 12 ms^{-1} are only highlighted as shades and contours.

Axis of the 950 hPa core is found to pass from Horn of Africa to Gulf of Kutch in Gujarat state of India. On the other hand, wind speed contours of 850 hPa core are stretching from Horn of Africa to east Arabian Sea with westerly-southwesterly winds flowing towards the west coast of India, Bay of Bengal and beyond. Ten-year average seasonal mean peak wind speed of the 850 hPa core is 18 ms^{-1} . Axis of the 850 hPa core is found to pass from Horn of Africa to Goa ($\sim 15^\circ \text{N}$) on the west coast of India. Significant differences in flow direction, spatial distribution and strength are noticeable between LLJ at 950 hPa and 850 hPa levels. It appears that wind flow at 950 hPa and at 850 hPa levels behaves differently and appears to have different characteristics. Figure 3 suggests that 950 hPa winds are stronger than 850 hPa winds over 2/3 of the Arabian Sea covering southwest, west, central, north and northeast parts. The difference is as high as 10 ms^{-1} in a small area off Oman coast. Over the south and the southeast Arabian Sea, 850 hPa winds are marginally ($\sim 1\text{--}3 \text{ ms}^{-1}$) stronger than 950 hPa winds.

To confirm the distinct wind flow pattern at 950 hPa revealed by the reanalysis data with an independent observation, near-surface wind estimated by a satellite-borne scatterometer is examined. Oceansat-2 scatterometer near-surface winds averaged during the summer monsoon season of 2010 is shown in Fig. 4. The spatial distribution of scatterometer winds of 2010 monsoon season matches well with the ten-year mean seasonal distribution of 950 hPa winds obtained from reanalysis data. In both datasets, winds are stronger off Somalia coast and west Arabian Sea. Winds are directed southwest to northeastward. Scatterometer winds confirm the existence of a distinct wind flow at 950 hPa flowing along the east African coast towards the north Arabian Sea. Near-surface scatterometer winds are relatively weaker than the reanalysis winds at 950 hPa possibly due to the surface friction. Spatial position of the ASB reported in literature¹⁵ matches well with the spatial position of the LLJ at 950 hPa reported in this work. Hence, we refer the LLJ at 950 hPa as the ASB of the LLJ. The 850 hPa winds which also emerge from the cross-equatorial flow along with 950 hPa flow near the Horn of Africa, crosses the Indian peninsula, takes a curved path over the Bay of Bengal and flows towards India as well as south China Sea. We refer this strong and organized wind flow at 850 hPa from the Horn of Africa to India via Bay of Bengal as B3 following the earlier study in literature¹⁵. Branching of the LLJ into ASB and B3 takes place over the southwest Arabian Sea. Meteorological community often considered the LLJ at 850 hPa (B3) for monsoon studies than the LLJ at 950 hPa (ASB).

Strong ASB pushes the surface water of the west Arabian Sea so that cold water from beneath comes to the surface to fill the displaced surface water. This process is known as ocean upwelling. Ocean upwelling over the Arabian Sea is more efficient off the coasts of Horn of Africa and Saudi Arabian Peninsula as no water is available from the land region on the west to replace the surface water pushed by the strong ASB. Hence bottom cold water has been brought up more efficiently by the ASB off the coasts of Africa and Saudi Arabia when compared to the open sea. So, a pool of cold SST is generated over southwest and west Arabian Sea. In Fig. 5, ten-year (2005–2014) average SST and 950 hPa wind during the JJAS season are shown for the study region. Cold pool of SST with temperature as low as 24°C is seen off Horn of Africa and Saudi Arabian Peninsula along the path of the ASB of the LLJ. Wind speed and SST contours suggest that SST tends to decrease on the entrance side of the ASB with accelerating winds whereas SST tends to increase on the exit side with decelerating winds. The cold-water upwelling is a positive feedback process in which increase in upwelling increases the meridional temperature gradient and the strength of the ASB, which in turn increases the upwelling further⁴¹.

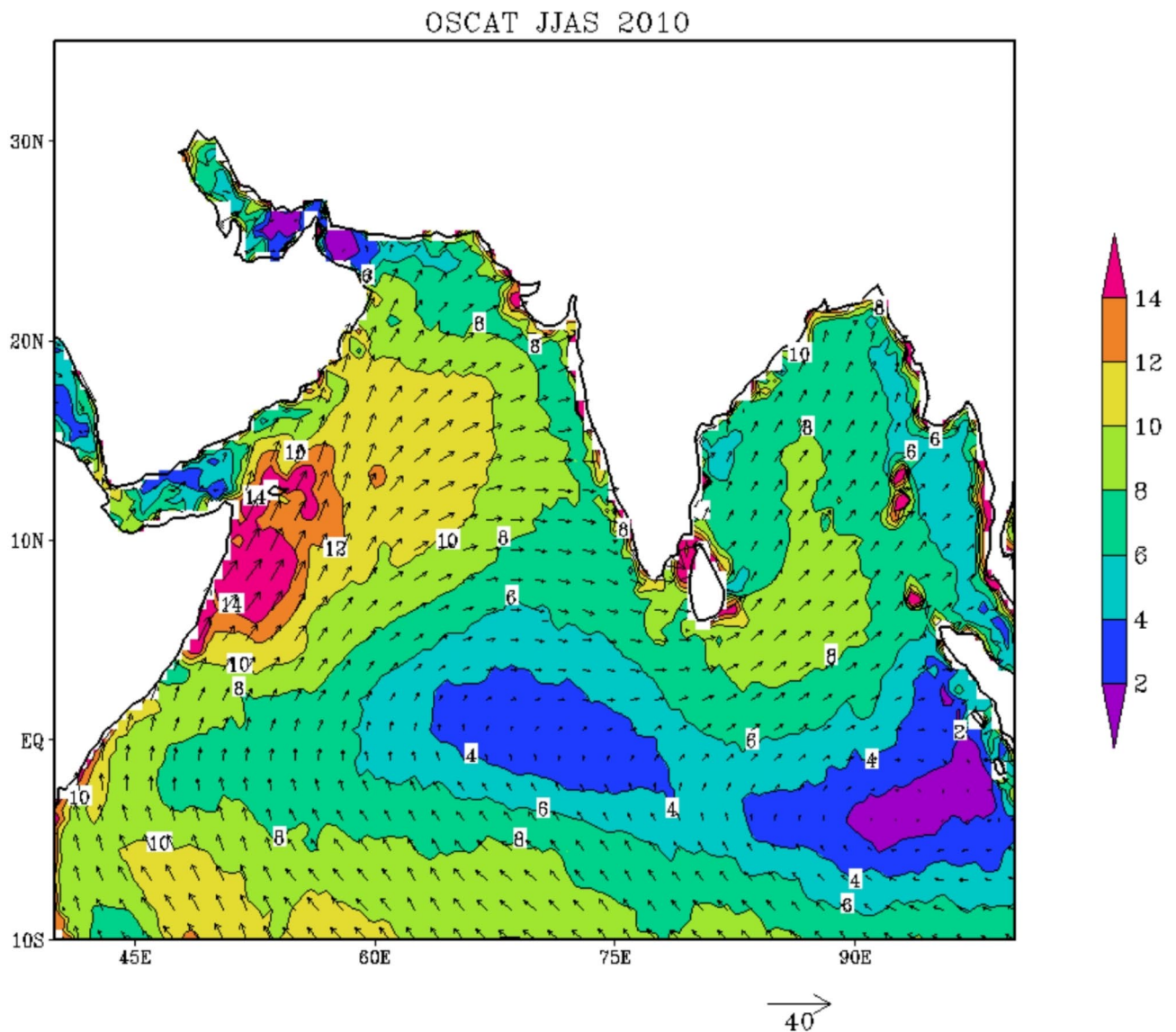


Fig. 4. Near-surface winds (ms^{-1}) observed by Oceansat-2 Ku-band scatterometer averaged during JJAS of 2010 [wind speed as shades and contours overlaid with wind vectors].

Roll clouds along the path of the ASB of the LLJ

In literature, roll clouds and closed convective cloud cells (C4) are visually identified from visible channel satellite imageries using the following subjective criteria: (i) Roll clouds appear as linear discrete cloud bands in the atmospheric boundary layer aligned nearly along the mean low level wind direction typically extending for about hundreds of kilometres along the wind direction and adjacent cloud bands separated by about tens of kilometres. They are found over the initial parts of the cold air outbreak flow. (ii) Further downstream of the cold air outbreak, C4 appear like hexagonal or cellular pattern of convective cloudiness in the atmospheric boundary layer and they have central cloudy area surrounded by clear-sky region.

Roll clouds are noticed over the Arabian Sea in high-resolution satellite visible channel imageries during JJAS^{33,40}. They are found along the flow path of the LLJ. In Fig. 6a,b, true colour imagery generated by merging band-1, band-3 and band-4 of Moderate Resolution Imaging Spectroradiometer (MODIS) onboard Terra satellite on 04 July 2002 is shown for the Arabian Sea along with a zoomed-in subset. Roll clouds are found over the central parts of the Arabian Sea. They appear initially as discrete parallel straight-line clouds and further away they break into individual clouds and appear as string of pearls. They are advected by prevailing wind. During their journey towards north and east Arabian Sea, they grow in size and become C4 if favourable instability and environmental conditions prevail. Once they reach the land, the linear structure is getting distorted. The zoomed-in figure (Fig. 6b) provides a magnified view of the roll clouds and their evolution. They are typically separated by a distance of about 10 km or less (~ 6.5 km on 04 July 2002) and stretch for about a few hundred kms. Visual examination of the MODIS imageries onboard Terra satellite during the ten-year study period (2005–2014) revealed that roll clouds are observed on 361 days out of 620 days (58% days) during the peak

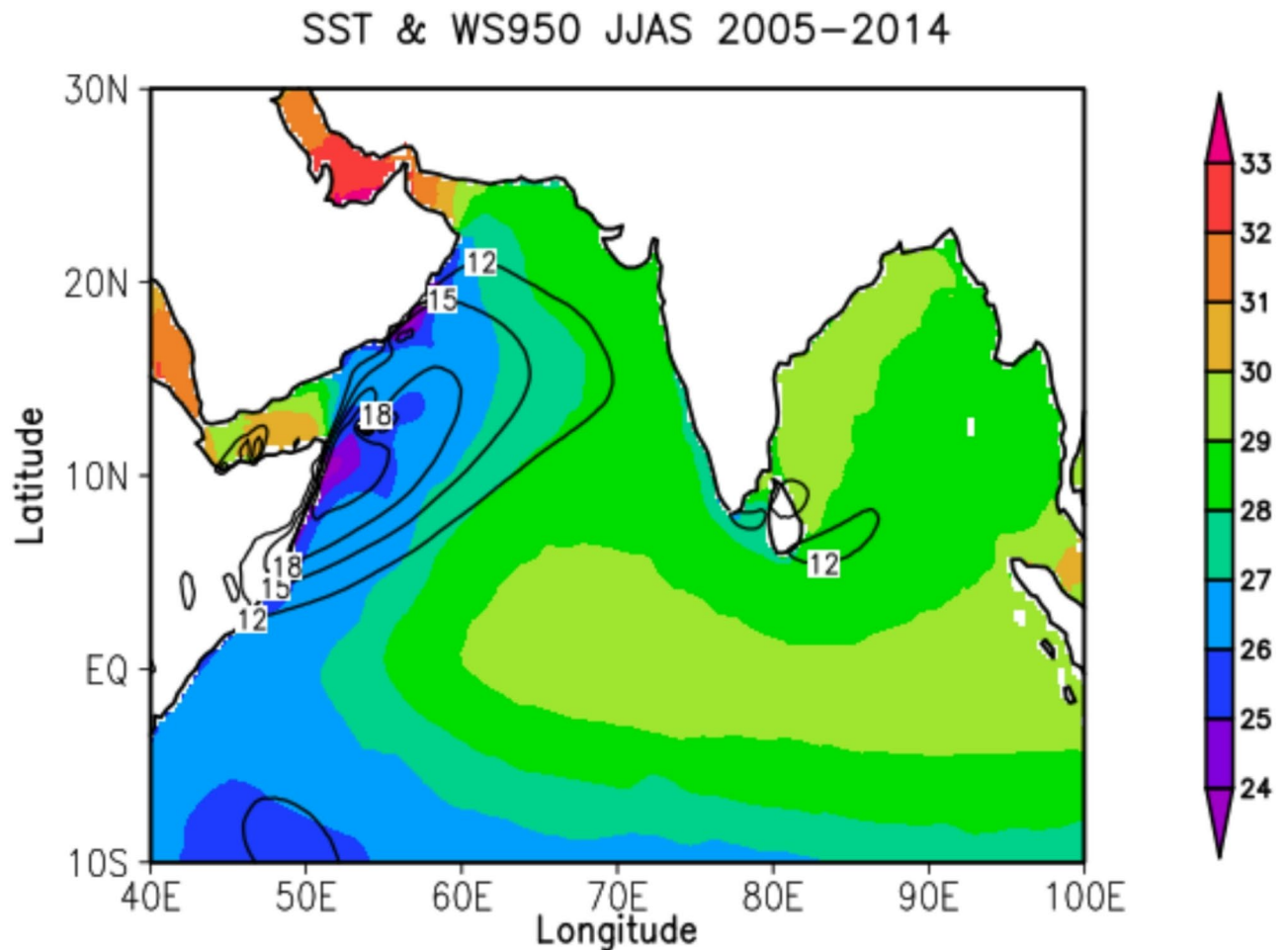


Fig. 5. Ten-year (2005–2014) average SST (°C) [in shades] and 950 hPa wind speed (ms^{-1}) [in contours] during JJAS over the study region. SST decreases on the entrance region of the ASB with increasing wind speed whereas SST increases on the exit region with decreasing wind speed.

monsoon season (July–August). List of Arabian Sea roll cloud days during the peak monsoon season of the 10-year study period is provided in Table 1. Because of the subjectivity involved in the visual identification, the roll cloud day identified is prone to human errors. MODIS imageries of all the roll cloud days of 2005 peak monsoon season (44 days) are provided as a supplementary figure (Fig. S1). Roll clouds are highly dynamic and evolving system. Satellite images reveal that their distribution is highly variable in space and time. Animations generated using half-hourly INSAT-3D geostationary satellite visible channel imageries over the Arabian Sea during the day-time of 31 July 2023 and 06 August 2023 are provided as supplementary materials (Ani. A1 and Ani. A2). These animations provide a better clarity on the advection of roll clouds, their transformation into C4 and spatio-temporal variability.

Over the west Arabian Sea, mean wind flow during the summer monsoon season is nothing but the ASB of the LLJ which causes cold water upwelling along its path. Due to the sensible heat flux exchange, winds blowing near the surface over cold SST region, acquire cold temperatures. Blowing of cold air on the exit side of the ASB over relatively warmer SST is analogous to the cold air outbreak occurring over the mid/high latitudes which generates thermally unstable atmospheric condition. Blowing of warm air on the entrance side with increasingly colder SST generates thermally stable atmospheric condition. In addition, blowing of warm air from Africa and Saudi Arabian Peninsula towards relatively cooler Arabian Sea also causes thermally stable atmosphere. Roll clouds are found on the exit region of the ASB with thermally unstable atmospheric condition. Two typical days of the peak summer monsoon season of 2023 viz., 31 July 2023 and 06 August 2023, during when roll clouds were observed without the obstruction of mid- or high-level clouds are considered for the case study. Visible Infrared Imaging Radiometer Suite (VIIRS) true colour imagery from NOAA-20 satellite for these two days are shown in Figs. 7a and 8a respectively. Clouds with varying sizes and shapes are seen over the Arabian Sea in these imageries. Over the southwest corner of the Arabian Sea (entrance region), cloud-free condition prevails on both these days. On the exit side of the ASB (central Arabian Sea) clouds in the form of unbroken straight lines (roll clouds) are seen initially. Further away along the flow path of the ASB, roll clouds break into individual clouds which appear as string of pearls. Further away, they further grow and become C4.

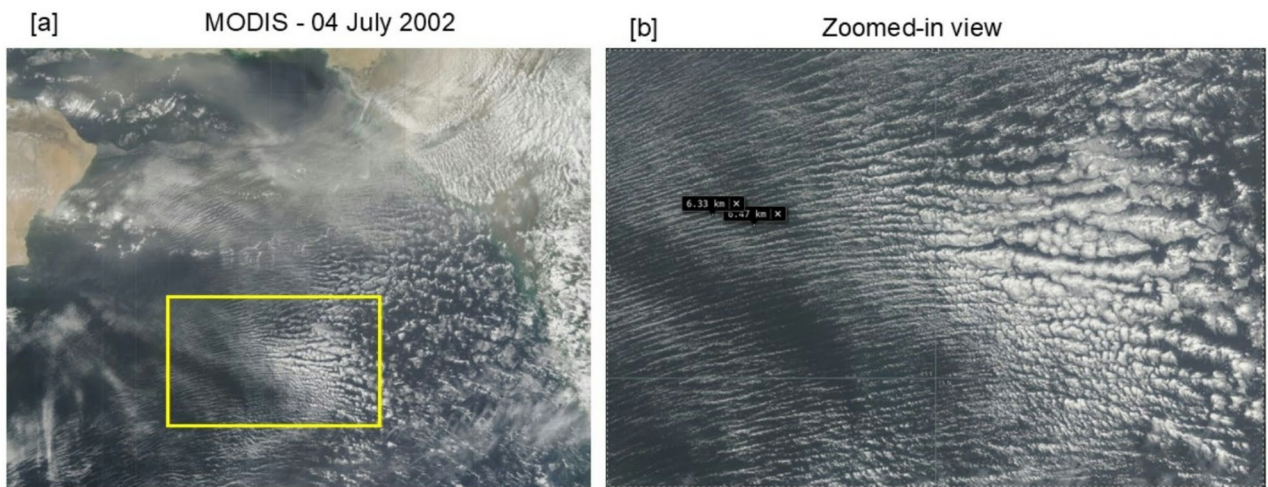


Fig. 6. (a) Spectacular display of roll clouds over the Arabian Sea in true colour imagery generated by merging band-1, band-3 and band-4 of MODIS payload onboard Terra satellite on 04 July 2002. (b) Zoomed-in view of the rectangular area highlighted in (a) showing roll clouds and their evolution into C4. Measurement at two places made using the measuring tool of the NASA Worldview website suggests that the distance between adjacent roll clouds is 6.33 km and 6.47 km. MODIS satellite image and its subset were directly downloaded from the NASA Worldview data portal available at <https://worldview.earthdata.nasa.gov/>. It is openly available without restriction to researchers.

Year	Roll cloud days during July–August	Total days	% Days
2005	01–15 J, 20 J, 22–27 J, 30 J–04 A, 06–18 A, 29–31 A	44	70.97
2006	01–20 J, 22 J, 25–27 J, 29 J, 31 J–04 A, 09–18 A, 20–24 A,	45	72.58
2007	01–23 J, 04–15 A, 20–21 A	37	59.68
2008	02–18 J, 20–25 J, 27–30 J, 01 A, 03 A, 07–10 A, 12–13 A, 19 A, 22 A, 26 A	38	61.29
2009	01–03 J, 05 J, 07 J, 10 J, 12–14 J, 20–22 J, 25 J–13 A, 15 A, 22–24 A, 26–29 A	40	64.52
2010	01–03 J, 06 J, 08–09 J, 12–13 J, 15–19 J, 21 J, 24–27 J, 29–31 J, 02–08 A, 10–16 A, 23–28 A	41	66.13
2011	01–02 J, 04–07 J, 11–15 J, 18 J, 20–26 J, 03–12 A	29	46.77
2012	01–04 J, 06–09 J, 11 J, 14–21 J, 24–29 J, 31 J, 03–04 A, 06 A, 09–11 A, 14–15 A, 18–19 A, 24 A, 27–28 A, 30–31 A	39	62.90
2013	01–04 J, 06–12 J, 14 J, 16–18 J, 20 J, 22 J, 28–29 J, 01 A, 05–06 A, 12 A, 28 A	24	38.71
2014	01 J, 04–09 J, 11 J, 13–15 J, 18–20 J, 26 J, 28 J, 30 J, 05 A, 09 A, 11 A, 14–17 A	24	38.71

Table 1. Roll clouds over the Arabian sea (Jul–Aug 2005–2014): number of roll cloud days visually identified using MODIS/Terra imageries during the peak monsoon season of the ten-year (2005–2014) study period. J represents July and A represents August in the table.

Thermal instability

To study the thermal instability conditions prevailing over the Arabian Sea, virtual potential temperature (θ_v) difference between two adjacent atmospheric levels (1000 hPa and 975 hPa) near the surface ($\Delta\theta_v = \theta_{v975} - \theta_{v1000}$) is computed. Air temperature, specific humidity and relative humidity data from ERA5 reanalysis are used for this computation. θ_v is calculated using equation-1; where θ is potential temperature, r_s is saturation mixing ratio and r_l is liquid water mixing ratio. θ is calculated using equation-2, where P_0 is the reference pressure (1000 hPa), T and P are air temperature and pressure of the atmospheric level, R_d is gas constant for dry air. C_p is specific heat capacity of dry air at constant pressure. r_s and r_l are calculated using equation-3 and equation-4 respectively; where q is specific humidity and RH is relative humidity.

$$\theta_v = \theta (1 + 0.62 r_s - r_l) \quad (1)$$

$$\theta = T \left(\frac{P_0}{P} \right)^{\frac{R_d}{C_p}} \quad (2)$$

$$r_s = \frac{q}{(1 - q) RH} \quad (3)$$

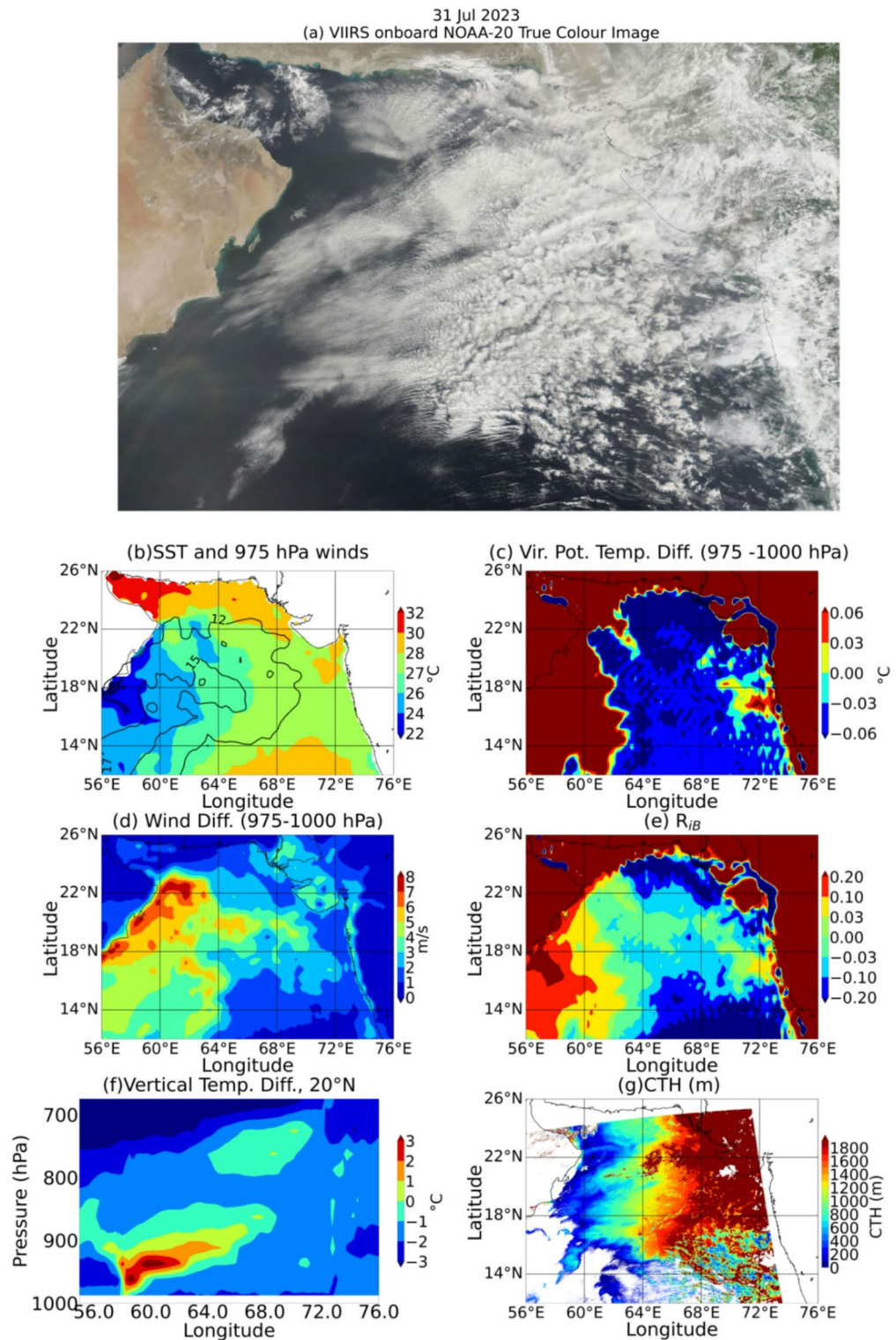


Fig. 7. (a) VIIRS onboard NOAA-20 true colour image of 31 July 2023 (b) SST(°C) in shades and 975 hPa wind speed (ms^{-1}) in contours, (c) Virtual potential temperature difference between 975 and 1000 hPa levels (°C) ($\theta_{v975} - \theta_{v1000}$) (d) wind difference (ms^{-1}) between 975 hPa and 1000 hPa levels (e) bulk Richardson number (f) Temperature difference (°C) between adjacent vertical pressure levels along 20°N and (g) Cloud top height (m) from VIIRS onboard NOAA-20 satellite for the same day. VIIRS/NOAA-20 satellite image was directly downloaded from the NASA Worldview data portal available at <https://worldview.earthdata.nasa.gov/>. It is openly available without restriction to researchers.

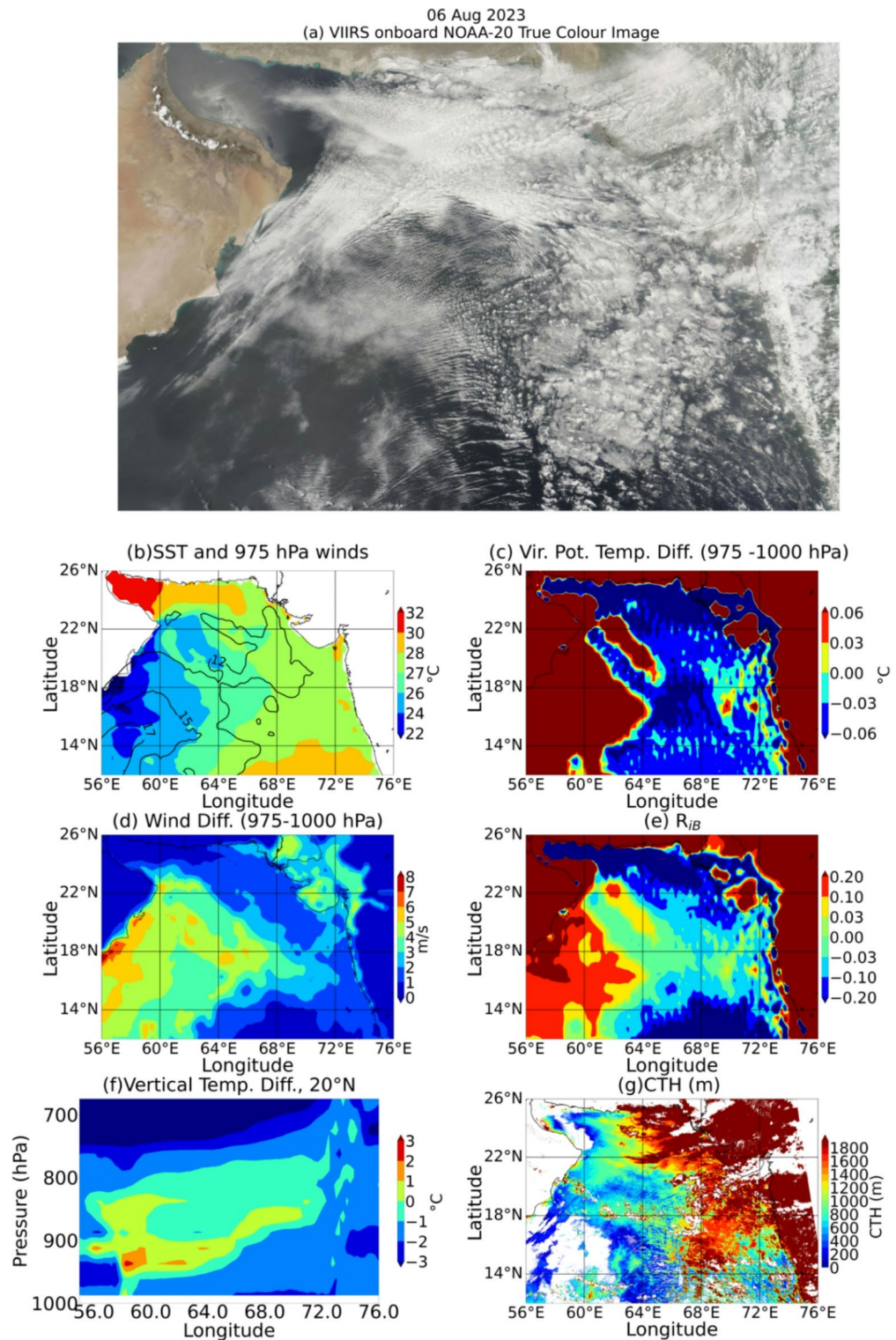


Fig. 8. Same as Fig. 7, but for 06 August 2023. VIIRS/NOAA-20 satellite image was directly downloaded from the NASA Worldview data portal available at <https://worldview.earthdata.nasa.gov/>. It is openly available without restriction to researchers.

$$r_l = \frac{q}{(1-q)} - r_s \quad (4)$$

Negative (positive) value of $\Delta\theta_v$ implies thermal instability (stability). Spatial distribution of $\Delta\theta_v$ for 31 July 2023 and 06 August 2023 are shown in Figs. 7c and 8c. Comparison of Figs. 7c and 8c with NOAA-20 VIIRS imageries (Figs. 7a and 8a) suggests that regions with positive $\Delta\theta_v$ on the entrance region of the ASB (over southwest and west Arabian Sea) are thermally stable and cloud-free on both these days. Roll clouds are observed on the exit region of the ASB (Figs. 7b and 8b) with marginally negative $\Delta\theta_v$ ranging from -0.03°C to -0.06°C . Roll clouds evolve further into individual convective cloud cells as they move away from the genesis region. As the SST over the north and the east Arabian Sea increases, $\Delta\theta_v$ becomes more negative ($< -0.06^\circ\text{C}$) and it is conducive for the roll clouds to evolve into C4.

Dynamic instability

Wind shear between two atmospheric levels near the surface is an important factor to understand the dynamic instability present in the boundary layer³⁰. Wind data from ERA5 reanalysis at 1000 hPa and 975 hPa are considered for the dynamic instability analysis. Dynamic instability is calculated using Eq. (5); where u and v are zonal and meridional wind components.

$$\text{Wind difference} = \sqrt{(u_{975} - u_{1000})^2 + (v_{975} - v_{1000})^2} \quad (5)$$

Spatial distribution of wind difference for 31 July 2023 and 06 August 2023 are shown in Figs. 7d and 8d respectively. Wind difference is found to vary between 0 and 9 ms^{-1} between these two levels over the Arabian Sea on these days. Roll clouds are found over moderate wind difference ($3\text{--}5\text{ ms}^{-1}$) regions over the central Arabian Sea. As roll clouds are advected further away by the ASB with weak wind difference, rolls evolve into C4. This is in agreement with the observations of earlier researchers²⁹, who noted that linear roll cloud structures can be found over moderate wind shear regions and closed convective cloud cells are found over weak wind shear regions.

Bulk Richardson number

To quantify the combined effect of thermal and dynamic instabilities, bulk Richardson number (R_{iB}) is computed for both 31 July 2023 and 06 August 2023. R_{iB} is a dimensionless quantity which is the ratio between turbulence due to thermal instability and turbulence due to dynamic instability in the atmospheric layer. This is mathematically represented by equation-6^{42,43}, where g is acceleration due to gravity in ms^{-2} , $z_2 - z_1$ is the difference in height between the top and bottom levels in metre. θ_{v2} and θ_{v1} are virtual potential temperatures at the top and at the bottom levels respectively. $\bar{\theta}_v$ is the average virtual potential temperature between these two levels. u_2 and u_1 are zonal winds at top and bottom levels. v_2 and v_1 are meridional winds at top and bottom levels.

$$R_{iB} = \frac{\text{Thermal instability}}{\text{Dynamic instability}} = \frac{g(z_2 - z_1)(\theta_{v2} - \theta_{v1})}{\bar{\theta}_v[(u_2 - u_1)^2 + (v_2 - v_1)^2]} \quad (6)$$

Since R_{iB} is measured over the ocean, virtual potential temperature is used in place of potential temperature in equation-6 to account for the moisture in the air⁴⁴. Spatial distribution of the bulk Richardson number calculated between 1000 hPa and 975 hPa levels on both these days is shown in Figs. 7e and 8e respectively. Cloud-free condition is found over statically stable regions with $R_{iB} > 0$. Linear roll clouds are found over near-neutral regions with $-0.03 < R_{iB} < 0$. Rolls evolve into closed convective cells over marginally unstable regions with $-0.1 < R_{iB} < -0.03$ on the exit side of the ASB (Figs. 7b and 8b). Above analysis was carried out for 12 days of 2023 peak monsoon season (29 July to 09 August) without the obstruction of roll clouds by mid- and upper-level clouds. Plots for the ten-days excluding the two days discussed in this section are provided as supplementary figure (Fig. S2). They also confirm that the roll clouds are found over near-neutral regions with bulk Richardson number ranging between -0.03 and 0.0 . Height of the lower tropospheric thermal inversion decides the upper limit of the roll clouds. Increase in inversion height towards north and east (Figs. 7f and 8f) facilitates vertical growth of roll clouds over the north and the east Arabian Sea. Cloud top height (CTH) obtained from NOAA-20 satellite (Figs. 7g and 8g) and vertical temperature difference indicating thermal inversion on these two days confirm that the vertical growth of the roll clouds and C4 gradually increases from the place of origin in accordance with the gradual increase in the height of the thermal inversion.

To have a quantitative estimation of these instability parameters on roll cloud formation, longitudinal variation of virtual potential temperature difference ($\Delta\theta_v$), wind difference and R_{iB} across the Arabian Sea are shown for 31 July 2023 and 06 August 2023 in Fig. 9. Different cloud regimes are marked for comparison purpose. This plot also confirms that roll clouds are formed when R_{iB} is marginally negative and cloud-free condition prevails where R_{iB} is positive. Similar analysis was made for 12 days of 2023 peak monsoon season (29 July to 09 August). They also show comparable changes in $\Delta\theta_v$, wind difference and R_{iB} over roll cloud and cloud-free regions. The longitudinal variation of R_{iB} for all these days (excluding 31 July and 06 August, which are already discussed) are provided as supplementary figure (Fig. S3). The R_{iB} ranges of -0.03 to 0 found in the roll cloud region during these ten-days are in agreement with the range of R_{iB} (-0.03 to -0.01) observed in earlier studies^{44,45}. Richardson number computation thus reveals that roll clouds are found over the exit region of the ASB with near-neutral to marginally unstable atmospheric conditions. They are advected by the ASB along its flow; occupy a wide region from the west Arabian Sea to about 12°N on the west coast of India.

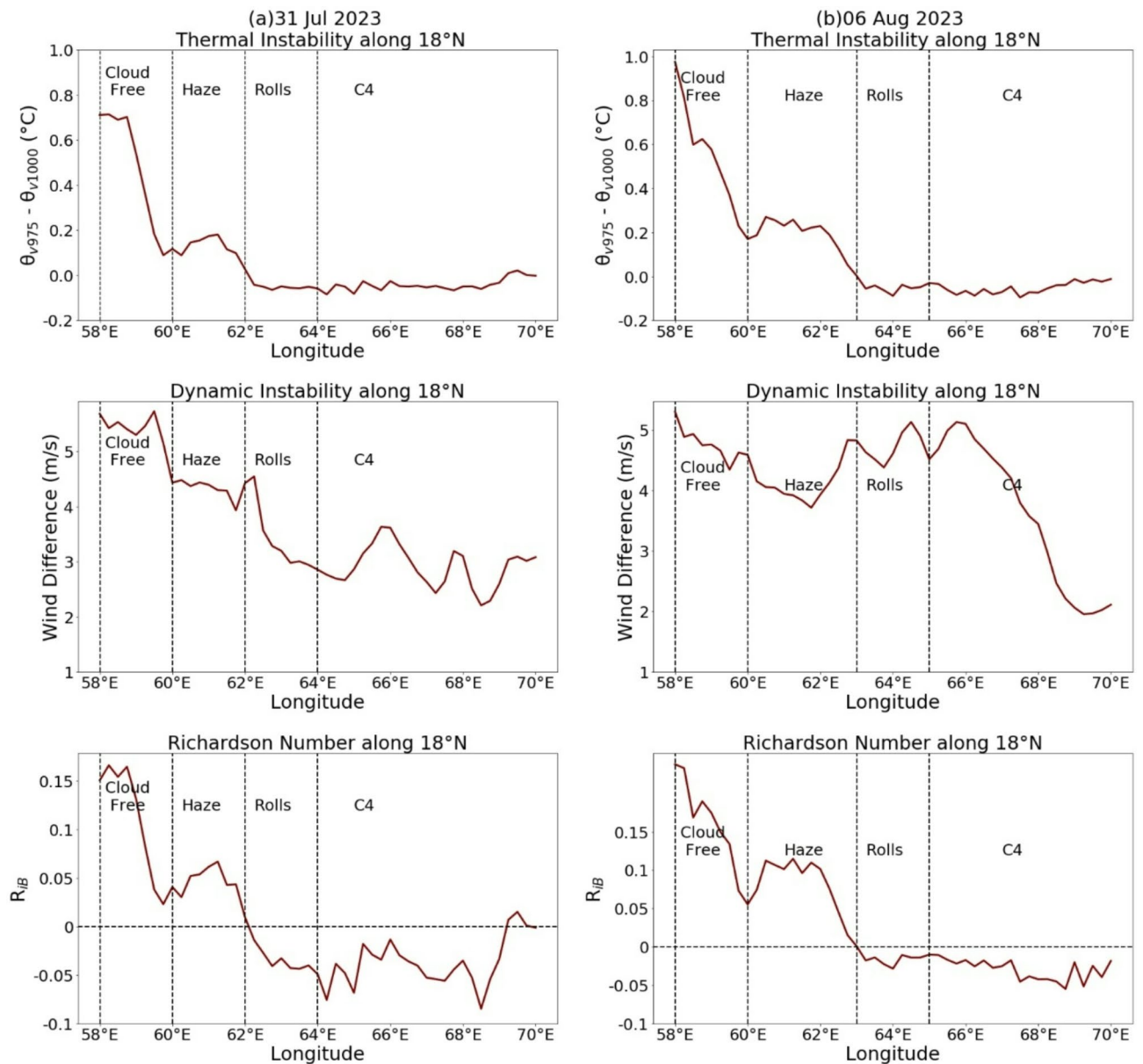


Fig. 9. Evolution of [top] virtual potential temperature difference ($\Delta\theta_v$, °C), [middle] wind difference (ms^{-1}) and [bottom] R_{iB} computed between 975 hPa and 1000 hPa for (a) 31 July 2023 and (b) 06 August 2023 along 18°N over the Arabian Sea.

Influence of roll clouds on the Indian summer monsoon activity

While roll clouds are advected from the genesis region by the ASB of the LLJ along its path, they grow in size (both vertical and horizontal), break into individual cells and evolve into C4 due to changes in instability and gradual increase in the height of the thermal inversion (Figs. 7f and 8f). It is to be remembered that the wavelength of the roll clouds (distance between adjacent cloudy or cloud-free regions) is directly proportional to the boundary layer/thermal inversion height⁴⁶. So, wavelength of roll clouds gradually increases as they grow vertically over the north and the east Arabian Sea with increased thermal inversion height.

Roll clouds and C4 are found to spread over a large part of the north Arabian Sea. Unlike the west coast of India, Gujarat and Rajasthan states of India and adjoining Pakistan are void of mountain chain to block the ASB of the LLJ. Hence roll clouds and C4 advected towards the north have free passage towards monsoon trough/Pakistan heat low. Due to the absence of mountains and forced lifting, these clouds do not yield significant rainfall over the west Indian states of Gujarat/Rajasthan and adjoining Pakistan. In contrast, roll clouds and C4 heading towards northern parts of Western Ghats (north of 12°N) are blocked by mountains. They may also enlarge in size during their journey towards Western Ghats. These clouds are unable to grow into deep convective clouds due to the suppression of cloud growth by thermal inversion (Figs. 7f and 8f). Roll clouds, continuously advected by the ASB are blocked by Western Ghats and getting accumulated and lifted on the

windward side. This stagnation and continuous supply of roll clouds are expected to yield continuous rainfall on northern parts of the west coast of India. Due to the stagnation by Western Ghats and distortion of roll structure on arriving land region, it is difficult to observe the roll cloud pattern (alternating rain and no-rain distribution) in rainfall data over the west coast of India.

Examination of the cloud data from ISCCP over the Indian summer monsoon region during July–August suggests that mostly low-level stratus and stratocumulus clouds are found over north Arabian Sea, Gujarat state of India and Pakistan whereas low- to mid-level nimbostratus clouds are found on the northern parts of the west coast of India (Fig. 10). ISCCP cloud data also suggests that clouds are shallow over the western Arabian Sea and their height increases eastward. Continuous transportation of roll clouds/closed convective cloud cells in the form of rain bearing nimbostratus clouds by the ASB is expected to provide continuous rainfall for several hours to days over northern parts of the west coast of India. Though stratus and stratocumulus clouds do not provide rainfall over Gujarat and Rajasthan states of India and Pakistan, they provide great relief from scorching summer by blocking incoming shortwave solar radiation.

In Fig. 11, time series of daily accumulated rainfall obtained from IMD averaged over the box bound between 73°E – 74°E and 16°N – 20°N located on the northern parts of the west coast of India is shown for the peak summer monsoon months (July–August) of 2023. During 29 July 2023 to 09 August 2023, roll clouds and C4 were present over north and northeast Arabian Sea without the obstruction of mid/upper-level clouds. Rainfall during these roll cloud/C4 days is marked in Fig. 11. During this period, light to moderate rainfall ranging from 5 mm day^{-1} to 25 mm day^{-1} was received over this box. This rainfall time series suggests that roll clouds and C4 provide light to moderate rainfall over northern parts of the west coast.

Conclusions

In this study, mechanism behind the formation of unique boundary layer roll clouds over the Arabian sea during the peak Indian summer monsoon season of July–August is studied. They are observed along the flow path of the ASB during the summer monsoon season. On the exit region of the ASB, cold air blows over the warmer SST region which results in thermal instability. The dynamical instability associated with the vertical wind shear of the ASB near the surface in association with thermal instability generates the roll clouds over the Arabian Sea. They are typically separated by a distance of about 10-km or less and stretch for a few hundred kms. To quantify the contribution of thermal and dynamic instabilities, bulk Richardson number is calculated between 975 hPa and 1000 hPa levels. It suggests that roll clouds are formed over the regions with near-neutral to marginally unstable atmospheric conditions. Roll clouds are advected by the ASB. They grow in size and break

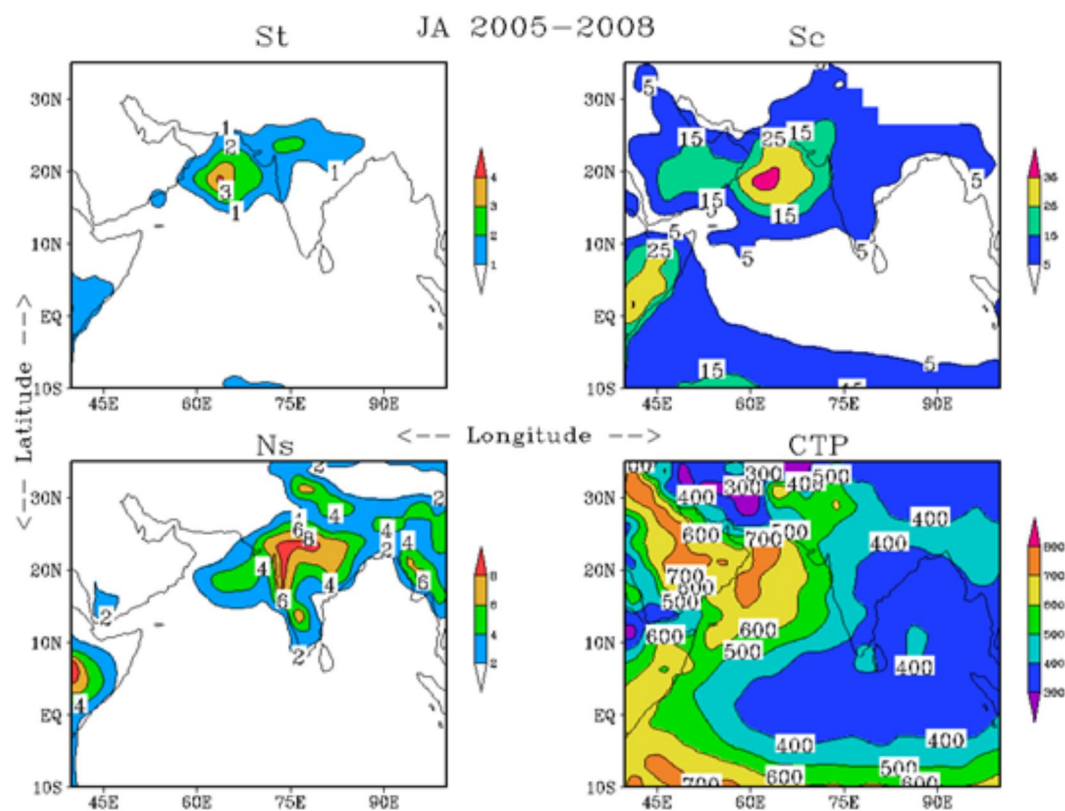


Fig. 10. Cloud cover amount (%) of stratus (St), stratocumulus (Sc) and nimbostratus (Ns) clouds averaged during the peak monsoon season (July–August) of four-year ISCCP data availability period (2005–2008) during the ten-year study period. Contour intervals are different for different clouds. Also, seasonal mean cloud top pressure (CTP, in hPa) averaged during the four-year period is shown.

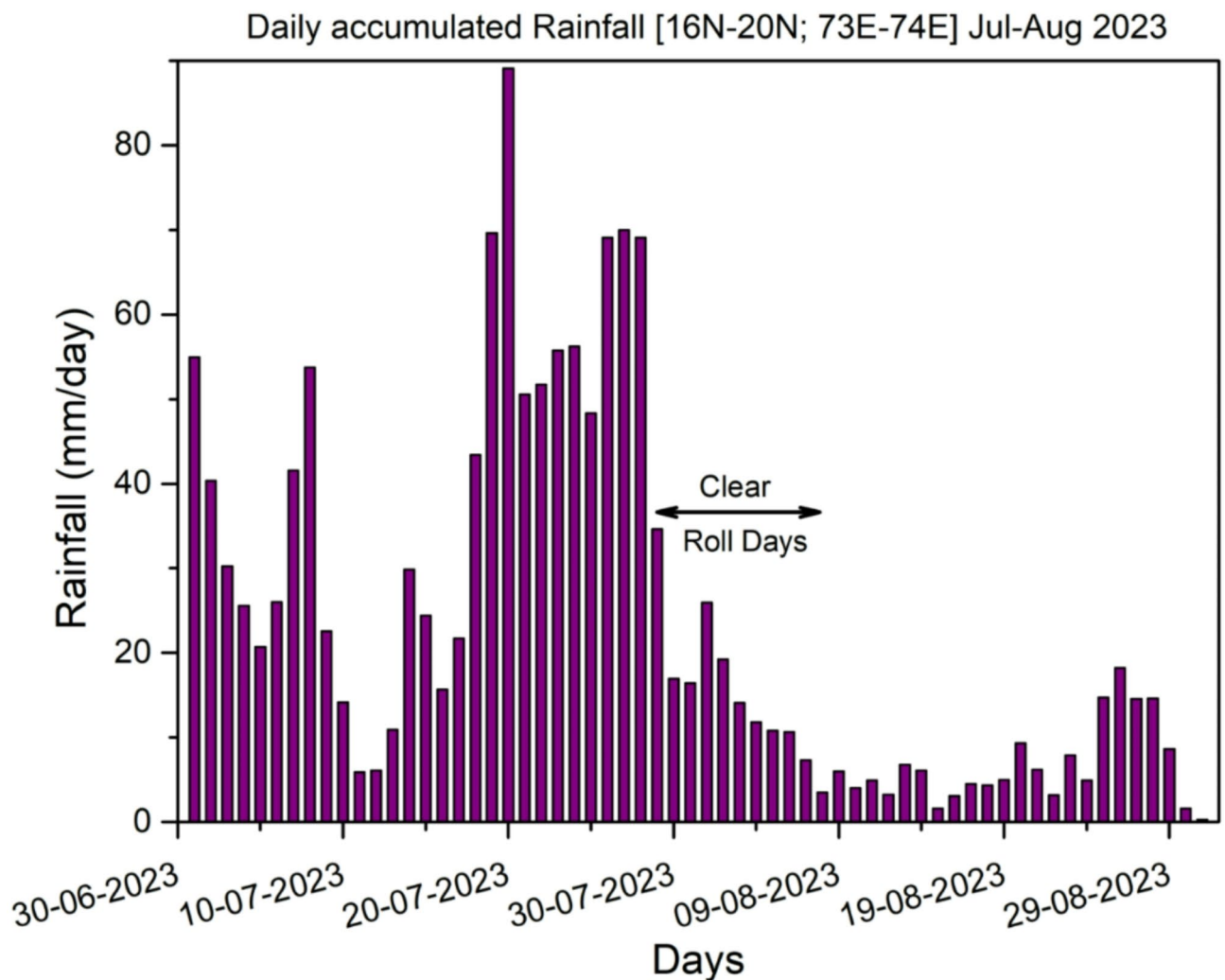


Fig. 11. Time series of daily accumulated IMD rainfall (mm day^{-1}) averaged over the box bound by 73°E – 74°E and 16°N – 20°N during the peak summer monsoon months (July–August) of 2023. Days during when roll clouds/C4 are seen over the Arabian Sea without the obstruction of mid- and high-level clouds are highlighted.

into individual cells and further evolve into closed convective cloud cells (C4) due to change in instability and gradual increase in the height of thermal inversion.

Roll clouds are formed far away from the Western Ghats mountain without the orographic lifting of monsoon winds. Roll clouds and C4 occupy a large part of the Arabian Sea. They are freely advected over the west Indian states of Gujarat and Rajasthan and adjoining Pakistan due to the absence of orography to block the flow of the ASB. They provide great relief from scorching sun by blocking the incoming solar radiation. But these clouds are blocked over northern parts of the west coast of India by Western Ghats. They are accumulated and lifted on the windward side of the Western Ghats and provide light to moderate rainfall. Arabian Sea roll clouds are unique in some aspects when compared to mid- and high-latitude roll clouds. They (i) persist for a season (ii) spread across a wider region and (iii) provide considerable rainfall where they are blocked or lifted by mountains. Arabian Sea is void of boundary layer meteorological observational network. Hence it is difficult to support the results obtained from ERA5 data with in-situ observations.

Present study is based on the visual inspection of satellite visible channel imageries which is bound to have inconsistency arising due to subjective identification of roll clouds and C4. This may introduce uncertainty in the total number of roll cloud days identified during the ten-year study period. Objective classification of roll cloud and non-roll cloud cases can minimize these inconsistencies. The objective method to identify roll clouds can be based on either the characteristic features of the roll clouds (distance between adjacent cloud bands, their horizontal length along mean wind direction) or the environmental conditions that support roll cloud formation (wind speed, wind shear, virtual potential temperature difference in the boundary layer). As summarized in earlier studies^{29–31,47}, above mentioned parameters have range of values which vary from region to region. This makes it difficult to have an objective criterion for roll cloud identification. At present the objective method of identifying roll clouds is an area of ongoing research. Preliminary attempts have been made to identify and

classify the marine low-level clouds using deep learning algorithms⁴⁸. Using the MODIS Aqua satellite imageries, they classified six types of marine low-level clouds (stratus, closed cellular convection, disorganized convection, open cellular convection, clustered cumulus convection, and suppressed cumulus convection) based on the morphological types and distinct spatial patterns. They claimed that the algorithm works well for identifying closed cellular convection. However, there is room to improve the deep learning algorithm to identify other marine low level cloud types like roll clouds. The deep learning algorithm can be improved by increasing the quantity of training data set. Rapidly increasing availability of meteorological observations by various satellites can serve as the training data to improve the deep learning algorithms.

Data

European Centre for Medium-Range Weather Forecasts (ECMWF) Reanalysis v5 (ERA5) provides various atmospheric variables on hourly and monthly time scales over a spatial grid of 0.25° lon. \times 0.25° lat. at various atmospheric pressure levels⁴⁹. For the present study daily zonal, meridional wind components at different pressure levels and sea surface temperature (SST) at 00:00 UTC (05:30 IST) during the summer monsoon season of 2005–2014 (ten-year study period) are used. ERA5 data (zonal and meridional wind components, specific humidity, relative humidity, air temperature at different pressure levels) of 2023 summer monsoon season at 08:00 UTC (13:30 IST) are also used for case studies as it coincides with the equatorial crossing time of NOAA-20 satellite used for the study. These data products are available online at <https://cds.climate.copernicus.eu>.

True colour images (1 km resolution, available from 2000 to present) generated by combining band-1, band-3 and band-4 of Moderate Resolution Imaging Spectroradiometer (MODIS) onboard Terra satellite (equatorial crossing at 10:30 LT) are used to visualise the roll clouds over Arabian sea during peak monsoon season of 2005–2014. High resolution (750 m resolution, available from 2018 to present) true colour images for the case studies are obtained from Visible Infrared Imaging Radiometer Suite (VIIRS) onboard National Oceanic and Atmospheric Administration (NOAA-20) satellite (equatorial crossing at \sim 13:30 LT). These images are created by combining VIIRS band I1, band M3, and band M4. Both MODIS Terra and VIIRS NOAA-20 true colour images are available for visualization on the NASA Worldview website (<https://worldview.earthdata.nasa.gov>). The cloud top height is obtained from VIIRS Level-2 cloud properties data (CLDPROP_L2_VIIRS_NOAA20) with a spatial resolution of 750 m. This data product is available online at NASA LAADS DAAC website (<https://ladsweb.modaps.eosdis.nasa.gov>).

Half-hourly visible channel imageries from INSAT-3D geostationary meteorological satellite were collected from Meteorological and Oceanographic Satellite Data Archival Centre (MOSDAC) of the Indian Space Research Organisation from <https://www.mosdac.gov.in>. Near-surface wind speed and direction above the ocean, measured by the scatterometer onboard Oceansat-2 satellite during 2010 are used in this study. These data were obtained from National Remote Sensing Centre, Hyderabad, India (<https://www.nrsc.gov.in>) and they are of very good quality⁵⁰. Daily high-resolution (0.25° lon. \times 0.25° lat.) gridded rainfall data of India Meteorological Department (IMD) for the ten-year study period have been used in the study⁵¹. Four year (2005–2008) gridded monthly cloud cover amount and cloud top pressure data available at 2.5° lon. \times 2.5° lat. resolution from the International Satellite Cloud Climatology Project (ISCCP) are used in this study^{52,53}.

Data availability

All the data used in the study were downloaded from the open source. Data availability details are provided in Results, Data and Acknowledgement sections.

Received: 22 September 2024; Accepted: 8 April 2025

Published online: 13 April 2025

References

1. Bunker, A. F. Interaction of the summer monsoon air with the Arabian Sea (preliminary analysis). Proceedings Symposium Meteorological Results, International Indian Ocean Expedition, Bombay, India. 22–26 (1965).
2. Joseph, P. V. & Raman, P. L. Existence of low level Westerly jet-stream over Peninsular India during July. *Mausam* **17**, 407–410 (1966).
3. Findlater, J. A major low level current the Indian ocean during Northern summer. *Quart. J. Roy Meteor. Soc.* **95**, 362–380 (1969).
4. Findlater, J. Observational aspects of the low-level cross-equatorial jet stream of the Western Indian ocean. *Pure Appl. Geophys.* **115**, 1251–1262 (1977).
5. Aneesh, S. & Sijikumar, S. Changes in the South Asian monsoon low level jet during recent decades and its role in the monsoon water cycle. *J. Atmos. Sol Terr. Phys.* **138–139**, 47–53 (2016).
6. Krishnamurti, T. N., Molinari, J. & Pan, H. L. Numerical simulation of the Somali jet. *J. Atmos. Sci.* **33**, 2350–2362 (1976).
7. Puranik, S. S., Ray, K. C. S., Sen, P. N. & Kumar, P. P. Impact of cross-equatorial meridional transport on the performance of the Southwest monsoon over India. *Curr. Sci.* **107**, 1006–1012 (2014).
8. Narayanan, S., Kottayil, A. & Mohanakumar, K. Monsoon low-level jet over the gateway of Indian summer monsoon: a comparative study for two distinct monsoon years. *Meteorol. Atmos. Phys.* **128**, 689–696 (2016).
9. Sarker, R. P. A dynamical model of orographic rainfall. *Mon Wea Rev.* **95**, 555–572 (1966).
10. Sarker, R. P. Some modification in a dynamical model of orographic rainfall. *Mon Wea Rev.* **95**, 673–684 (1967).
11. Grossman, R. L. & Durran, D. R. Interaction of low-level flow with the Western Ghat mountains and offshore convection in the summer monsoon. *Mon Wea Rev.* **112**, 652–672 (1984).
12. Maheskumar, R. S. et al. Mechanism of high rainfall over the India West Coast region during the monsoon season. *Clim. Dyn.* **43**, 1513–1552 (2014).
13. Tawde, S. A. & Singh, C. Investigation of orographic features influencing Spatial distribution of rainfall over the Western Ghats of India using satellite data. *Int. J. Climatol.* **35**, 2280–2293 (2015).
14. Wilson, S. S., Mohanakumar, K. & Roose, S. A study on the structural transformation of monsoon low level jet stream on its passage over the South Asian region. *Pure Appl. Geophys.* **176**, 3681–3695 (2019).

15. Fu, C., Fletcher, J. & Slutz, R. The structure of the Asian monsoon surface wind field over the ocean. *J. Cli Appl. Meteor.* **22**, 1242–1252 (1983).
16. Gupta, S. K., Deshpande, R. D., Bhattacharya, S. K. & Jani, R. A. Ground water $\delta^{18}\text{O}$ and δD from central Indian Peninsula: influence of the Arabian sea and the Bay of Bengal branches of the summer monsoon. *J. Hydrol.* **303**, 38–55 (2005).
17. Sinha, N., Chattopadhyay, R. & Chakraborty, S. Bay of Bengal branch of Indian summer monsoon and its association with Spatial distribution of rainfall patterns over India. *Theor. Appl. Climatol.* **137**, 1895–1907 (2019).
18. Das, D., Mondal, P., Saha, P. & Chaudhuri, S. Investigation on the Bay of Bengal branch of summer monsoon during normal and delayed onset over gangetic West Bengal. *Meteorol. Atmos. Phys.* **131**, 957–973 (2019).
19. Sathiyamoorthy, V. A study on the anomalous TOA net radiative warming by clouds in a sub-region within the Indian summer monsoon region. *Adv. Spa Sci.* **70**, 3638–3648 (2022).
20. Kuettner, J. P. The band structure of the atmosphere. *Tellus* **11**, 267–294 (1959).
21. Kuettner, J. P. Cloud bands in the atmosphere. *Tellus* **23**, 404–425 (1971).
22. Brown, R. A. Longitudinal instabilities and secondary flows in the planetary boundary layer: A review. *Rev. Geophys.* **18**, 683–697 (1980).
23. Kuo, H. L. Perturbations of plane couette flow in stratified fluid and origin of cloud streets. *Phys. Fluids.* **6**, 195–211 (1963).
24. Asai, T. Three-dimensional features of thermal convection in a plane couette flow. *J. Meteor. Soc. Japan.* **48** (1), 18–29 (1970a).
25. Asai, T. Stability of plane parallel flow with variable vertical shear and unstable stratification. *J. Meteorol. Soc. Japan.* **48**, 129–139 (1970b).
26. Asai, T. Thermal instability of a shear flow turning the direction with height. *J. Meteor. Soc. Japan.* **50**, 525–532 (1972).
27. Brown, R. A. A secondary flow model for the planetary boundary layer. *J. Atmos. Sci.* **27**, 742–757 (1970).
28. Brown, R. A. & Liu, W. T. An operational large-scale marine planetary boundary layer model. *J. Appl. Meteor.* **21**, 261–269 (1982).
29. Etling, D. & Brown, R. A. Roll vortices in the planetary boundary layer: A review. *Boundary-Layer Meteorol.* **65**, 215–248 (1993).
30. Atkinson, B. W. & Zhang, J. W. Mesoscale shallow convection in the atmosphere. *Rev. Geophys.* **34**, 403–431 (1996).
31. Weckwerth, T. M., Wilson, J. W., Wakimoto, R. M. & Crook, N. A. Horizontal convective rolls: determining the environmental conditions supporting their existence and characteristics. *Mon Wea Rev.* **125**, 505–526 (1997).
32. Young, G. S., Kristovich, D. A. R., Hjelmfelt, M. R. & Foster, R. C. Rolls, streets, waves, and more: A review of quasi-two-dimensional structures in the atmospheric boundary layer. *Bull. Amer Meteor. Soc.* **83** (7), 997–1002 (2002).
33. Sathiyamoorthy, V. & Rana, P. Cloud streets occurrence over the Arabian sea during summer monsoon season. *Int. J. Emer Tech.* **11** (1), 297–304 (2020).
34. Sathiyamoorthy, V., Pal, P. K. & Joshi, P. C. Influence of the upper tropospheric wind shear upon cloud radiative forcing in the Asian monsoon region. *J. Clim.* **17**, 2725–2735 (2004).
35. Brummer, B. & Pohlmann, S. Wintertime roll and cell convection over Greenland and Barents sea regions: A climatology. *J. Geophys. Res: Atmos.* **105**, 15559–15566 (2000).
36. Wu, P. & Ovchinnikov, M. Cloud morphology evolution in Arctic cold-air outbreak: two cases during COMBLE period. *J. Geophys. Res: Atmos.* **127**, e2021JD035966 (2022).
37. Weston, K. J. An observational study of convective cloud streets. *Tellus* **32**, 433–438 (1980).
38. Walter, B. A. Wintertime observations of roll clouds over the Bering sea. *Mon Wea Rev.* **108**, 2024–2031 (1980).
39. Chen, Y., Yuan, H. & Gao, S. A high-resolution simulation of roll convection over the yellow sea during a cold air outbreak. *J. Geophys. Res: Atmos.* **124**, 10608–10625 (2019).
40. Sathiyamoorthy, V. et al. Characteristics of low clouds over the Arabian sea. *J. Geophys. Res: Atmos.* **118**, 13489–13513 (2013).
41. Saha, K. R. Some aspects of the Arabian sea summer monsoon. *Tellus* **26**, 464–476 (1974).
42. Stull, R. B. *An Introduction To Boundary Layer Meteorology* (RB Stull (Springer Netherlands, 1988).
43. Garratt, J. R. *The Atmospheric Boundary Layer* (Cambridge University Press, 1992).
44. Brooks, I. M. & Rogers, D. P. Aircraft observations of boundary layer rolls off the Coast of California. *J. Atmos. Sci.* **54**, 1834–1849 (1997).
45. LeMone, M. A. The structure and dynamics of horizontal roll vortices in the planetary boundary layer. *J. Atmos. Sci.* **30**, 1077–1091 (1973).
46. Kelly, R. D. Horizontal roll and Boundary-Layer interrelationships observed over lake Michigan. *J. Atmos. Sci.* **41**, 1816–1826 (1984).
47. Weckwerth, T. M., Horst, T. W. & Wilson, J. W. An observational study of the evolution of horizontal convective rolls. *Mon Wea Rev.* **127** (2), 179 (1999).
48. Yuan, T. et al. Applying deep learning to NASA MODIS data to create a community record of marine low-cloud mesoscale morphology. *Atmospheric Meas. Tech. Discuss.* **13** (6), 997 (2020).
49. Hersbach, H. et al. The ERA5 global reanalysis. *Quart. J. Roy Meteor. Soc.* **146**, 1999–2049 (2020).
50. Sathiyamoorthy, V., Sikkakolli, R., Gohil, B. S. & Pal, P. K. Intra-seasonal variability in Oceansat-2 scatterometer sea-surface winds over the Indian summer monsoon region. *Meteorol. Atmos. Phys.* **117**, 145–152 (2012).
51. Pai, D. S. et al. Development of a new high Spatial resolution ($0.25^\circ \times 0.25^\circ$) long period (1901–2010) daily gridded rainfall data set over India and its comparison with existing data sets over the region. *Mausam* **65**, 1–18 (2014).
52. Schiffer, R. A. & Rossow, W. B. The international satellite cloud climatology project (ISCCP): the first project of the world climate research programme. *Bull. Amer Meteor. Soc.* **64**, 779–784 (1983).
53. Rossow, W. B. & Schiffer, R. A. Advances in Understanding clouds from ISCCP. *Bull. Amer Meteor. Soc.* **80**, 2261–2288 (1999).

Acknowledgements

Authors sincerely thank the Director, Space Physics Laboratory, Vikram Sarabhai Space Centre, Thiruvananthapuram for his keen interest and useful discussions during the study. One of the authors, BS thankfully acknowledges the research fellowship offered by Vikram Sarabhai Space Centre, Thiruvananthapuram. Authors acknowledge (i) ECMWF for providing ERA5 datasets (<https://cds.climate.copernicus.eu>), (ii) MOSDAC (<https://www.mosdac.gov.in>) for INSAT-3D satellite imageries, (iii) NASA Worldview (<https://worldview.earthdata.nasa.gov>) for images of MODIS onboard Terra satellite and VIIRS onboard NOAA-20, (iv) NASA LAADS DAAC (<https://ladsweb.modaps.eosdis.nasa.gov>) for VIIRS cloud top height data, (v) National Remote Sensing Centre, India (<https://www.nrsc.gov.in>) for Oceansat-2 scatterometer data (vi) International Satellite Cloud Climatology Project for cloud data and (vii) India Meteorological Department (IMD) for rainfall data. The plots are generated using the open-source programming language python-version 3.9.18 (<https://www.python.org/>) and Grid Analysis and Display System (GrADS, <http://cola.gmu.edu/grads/>).

Author contributions

B. S. & V. S. contributed to the conception and design of the study. Material preparation, data collection and analysis were performed by both.

Declarations

Competing interests

The authors declare no competing interests.

Additional information

Supplementary Information The online version contains supplementary material available at <https://doi.org/10.1038/s41598-025-97849-9>.

Correspondence and requests for materials should be addressed to V.S.

Reprints and permissions information is available at www.nature.com/reprints.

Publisher's note Springer Nature remains neutral with regard to jurisdictional claims in published maps and institutional affiliations.

Open Access This article is licensed under a Creative Commons Attribution-NonCommercial-NoDerivatives 4.0 International License, which permits any non-commercial use, sharing, distribution and reproduction in any medium or format, as long as you give appropriate credit to the original author(s) and the source, provide a link to the Creative Commons licence, and indicate if you modified the licensed material. You do not have permission under this licence to share adapted material derived from this article or parts of it. The images or other third party material in this article are included in the article's Creative Commons licence, unless indicated otherwise in a credit line to the material. If material is not included in the article's Creative Commons licence and your intended use is not permitted by statutory regulation or exceeds the permitted use, you will need to obtain permission directly from the copyright holder. To view a copy of this licence, visit <http://creativecommons.org/licenses/by-nc-nd/4.0/>.

© The Author(s) 2025